A Time-Dependent Lateral Boundary Scheme for Limited-Area Primitive Equation Models

DONALD J. PERKEY[1] AND CARL W. KREITZBERG

Drexel University, Philadelphia, Pa. 19104

(Manuscript received 25 September 1975, in revised form 30 January 1976)

ABSTRACT

Before high-resolution numerical models can be of use operationally, they must be restricted to a limited domain, thus necessitating lateral boundary conditions which allow the changes outside the limited domain to influence the results while not contaminating the forecast with spurious boundary-reflected energy. Such a set of time-dependent lateral boundary conditions are presented in this paper. This boundary condition set is investigated using the linear analytic and finite-difference advection equations, the nonlinear finite-difference shallow-water equations, and the hydrostatic primitive equations.

The results illustrate how the boundary condition transforms long- and medium-length interior advective and gravity waves into short waves which can then be removed by a low pass filter, thereby giving the appearance that the exiting wave simply passed through the boundary. The results also indicate that large-scale advective and gravity waves enter the forecast domain with little degradation. Thus, from the tests performed, the described boundary condition scheme yields a practical solution for prescribing time-dependent lateral boundaries for a limited-area model.

1. Introduction

When large-scale conditions indicate the need for special high-resolution computations, detailed short-range numerical forecasts can be operationally practical and effective only if they utilize the latest large-scale observations and model calculations applicable to a limited area. Because of the limited-area nature of these forecasts, lateral boundary conditions are necessary. Thus, the method of specifying these boundary conditions so that the limited-area forecast is influenced by the large-scale forcing and is not contaminated by erroneous reflection of energy from the boundary is of considerable importance.

Several authors (Davies, 1972; Sundström, 1973; Oliger and Sundström, 1976; and others) have demonstrated that great care must be taken to insure boundary conditions which are mathematically well-posed for the hydrostatic primitive equations; however, to date no satisfactory solution to the problem has been demonstrated. Such well-posed conditions must not only be numerically stable but must be nonreflective in order to be of practical value.

Various practical formulations of boundary conditions have been used and discussed in the literature. Shapiro and O'Brien (1970) using the filtered equations, and Williamson and Browning (1974) using the primitive equations, designate a region as inflow or outflow based on whether the wind normal to the boundary is in or out of grid domain. The boundary conditions are then based on this designation with large-scale quantities predominantly determining the conditions in inflow regions and model quantities predominantly determining the conditions in outflow regions. This scheme experiences difficulty when the large-scale winds specified at the boundary indicate inflow, while the model-calculated winds one grid interval interior to the boundary indicate outflow.

This paper develops a practical boundary technique which allows useful limited-area forecasts to be made in spite of the mathematically ill-posed nature of the problem. The set of time-dependent lateral boundary conditions presented allows large-scale waves to enter the limited-area forecast domain but does not allow exiting large- or small-scale waves to be reflected with sufficient amplitude to ruin the results. Section 2 describes the system and discusses some of its implications. Section 3 investigates the behavior of the system using both linear analytic and nonlinear finite-difference representations of the advective wave. Section 4 discusses the boundary conditions with respect to the shallow-water equations and gravity waves. Finally, Section 5 presents results from tests using a dry, two-dimensional primitive equation model.

2. The lateral boundary conditions

The boundary conditions consist of large-scale time-varying tendencies linearly combined with model-

[1] Present affiliation: National Center for Atmospheric Research, Boulder, Colo. 80303. The National Center for Atmospheric Research is sponsored by the National Science Foundation.

calculated tendencies. The large-scale conditions may be either generated by a large-scale model for real-time forecasts or calculated from real-data analysis for research studies. In either case it is usually necessary to interpolate the large-scale data in both time and space in order to obtain the boundary condition tendencies.

The prediction of any dependent variable χ can be written as follows:

$$\chi_n(I)=\chi_p(I)+W(I)\left.\frac{\partial \chi_m}{\partial t}\right|_I \Delta t+[1-W(I)]\left.\frac{\partial \chi_{ls}}{\partial t}\right|_I \Delta t, \quad (1)$$

where the subscripts n and p denote the "new" value after the boundary condition and the "previous" value at a former time. The ls denotes the large-scale specified tendency of χ, and m, the model-calculated tendency. The values of the weighting coefficients W are given below:

$$W(I)=\begin{cases}0.0 \text{ for } I=\text{the boundary grid points,}\\ 0.4 \text{ for } I=\text{the boundary}-1 \text{ grid points,}\\ 0.7 \text{ for } I=\text{the boundary}-2 \text{ grid points,}\\ 0.9 \text{ for } I=\text{the boundary}-3 \text{ grid points,}\\ 1.0 \text{ for } I=\text{all other interior grid points.}\end{cases} \quad (2)$$

Thus, the value at the boundaries is completely specified by the large-scale imposed value, while at a distance 4Δ from the boundaries, the variable value is identical to the model-calculated value. If $\partial \chi_{ls}/\partial t$ is zero, (1) and (2) are similar to the "sponge" boundary condition used by Kesel and Winninghoff (1972).

These equations are also similar to the boundary scheme used by the National Meteorological Center (NMC) limited-area fine-mesh model (LFM) (Cooley, 1973). The LFM uses a blend of the LFM and the six-layer hemispheric PE model tendencies on both u and v wind components, temperature, and mass fields. The six-layer PE model tendencies are calculated from six-hourly PE history fields biquadradically interpolated in space to the LFM grid points. The weighting is as follows:

$$W(I)=\begin{cases}0.0 \text{ for } I=\text{the boundary grid points,}\\ 0.33 \text{ for } I=\text{the boundary}-1 \text{ grid points,}\\ 0.67 \text{ for } I=\text{the boundary}-2 \text{ grid points,}\\ 1.0 \text{ for } I=\text{all other interior grid points.}\end{cases}$$

The implications of (1) and (2) can be illustrated using the linear advection equation,

$$\frac{\partial h_m}{\partial t}=-c\frac{\partial h}{\partial x}, \quad (3)$$

where c is a constant and h is referred to as height. In the absence of external forcing, Eq. (1) may be written in continuous space as

$$\frac{\partial h}{\partial t}=W(x)\frac{\partial h_m}{\partial t}, \quad (4)$$

where $W(x)$ is an analytic function which fits the distribution of $W(I)$. Thus, Eq. (3) can now be written as

$$\frac{\partial h}{\partial t}+cW(x)\frac{\partial h}{\partial x}=0. \quad (5)$$

It can be seen that the effect of the boundary condition is to reduce the phase velocity of a disturbance to zero as it approaches the boundary. Therefore, in effect, the boundary condition as given by Eqs. (1) and (3) alters the basic advection equation in such a way that the ill-posedness of the boundaries is no longer an issue.

Eq. (5) also implies that the disturbance's wavelength must decrease and the gradient of h must increase in the boundary region. This necessitates the use of a smoothing device in this region.

Note that for cases which do not require the merger with externally specified conditions at the boundaries, the boundary grid points are superfluous and could be eliminated, thereby saving computer resources. However, it does create a problem—how should the model tendencies at the new reduced domain boundaries be evaluated? One solution is to extrapolate the interior model tendencies to the boundaries, i.e.,

$$\left.\frac{\partial \chi}{\partial t}\right|_B=\left.\frac{\partial \chi}{\partial t}\right|_{B-1}+\left[\left.\frac{\partial \chi}{\partial t}\right|_{B-1}-\left.\frac{\partial \chi}{\partial t}\right|_{B-2}\right],$$

where the subscript B indicates the new lateral boundary grid points. Thus, Eqs. (1) and (2) reduce to

$$\chi_n(I)=\chi_p(I)+W(I)\left.\frac{\partial \chi_m}{\partial t}\right|_I \Delta t,$$

where

$$W(I)=\begin{cases}0.4 \text{ for } I=\text{the new boundary grid points,}\\ 0.7 \text{ for } I=\text{the new boundary}-1 \text{ grid points,}\\ 0.9 \text{ for } I=\text{the new boundary}-2 \text{ grid points,}\\ 1.0 \text{ for } I=\text{all other interior grid points.}\end{cases}$$

There is a minor difference between this modified boundary condition (referred to as a "porous sponge" condition) and the complete condition of Eqs. (1) and (2) with $\partial \chi_{ls}/\partial t=0$ (the "sponge" condition). Fig. 1 depicts this difference. Notice that the extrapolation condition allows the tendency at "porous sponge" point B to float slightly in response to the interior of the grid, while the "sponge" condition with the boundaries tied down reduces the response of the same point.

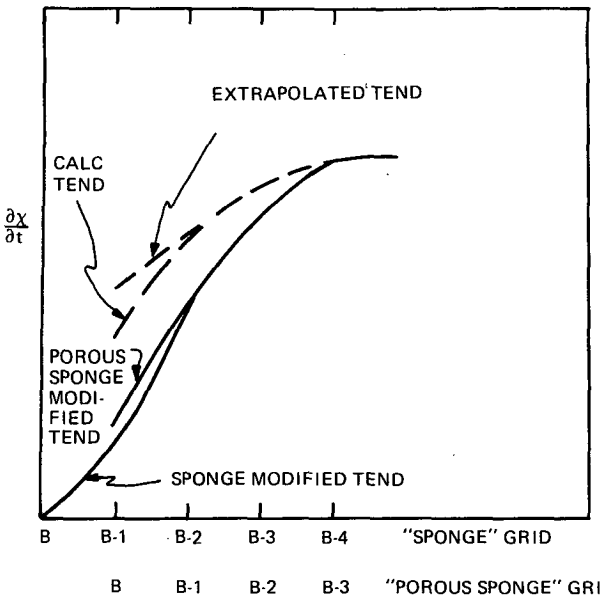

FIG. 1. Distinction between "sponge" and "porous sponge" boundary conditions. The dashed lines show a model-calculated tendency and an extrapolation-calculated tendency. The solid lines show the "sponge" and "porous sponge" modified tendencies.

The "porous sponge" scheme has been used in many integrations and has proven to remain stable and thus useful in saving computer resources when no external forcing is available.

3. Advective wave tests

a. Zero large-scale tendencies

For tests described in this section, the large-scale boundary tendencies remain zero, i.e., the boundaries are held constant throughout the forecast. Thus, only the sponge boundary condition remains:

$$\chi_n(I)=\chi_p(I)+W(I)\left.\frac{\partial \chi_m}{\partial t}\right|_I \Delta t, \tag{6}$$

where $W(I)$ is given by Eq. (2).

1) LINEAR ANALYTIC SOLUTION

To further illustrate the implications of the boundary conditions on advective waves, it is noted that (5) is a simple, linear, first-order partial differential equation. Transforming it into an ordinary differential by comparing it with

$$\frac{\partial h}{\partial t}dt+\frac{\partial h}{\partial x}dx=dh$$

yields a family of characteristic curves:

$$dt=\frac{dx}{cW(x)}. \tag{7}$$

These x-t space curves are solutions along which $dh=0$.

Note that $W(x)$ can be approximated by

$$W(x)\approx\begin{cases}\sin(2\pi x/L_1), & 0\leqslant x\leqslant L_1/4,\\ 1, & L_1/4<x<L_2,\\ \cos[2\pi(x-L_2)/L_1], & L_2\leqslant x\leqslant L,\end{cases} \tag{8}$$

where $L_1=16\Delta x$, $L_2=L-(L_1/4)$ and L is the domain size. Thus, integrating (7) after substitution of (8) yields

$$t-t_0=\begin{cases}\dfrac{L_1}{2\pi c}\ln\left[\dfrac{\tan\frac{\pi x}{L_1}}{\tan\frac{\pi x_0}{L_1}}\right], & 0\leqslant x\leqslant L_1/4,\\ (x-x_0)/c, & L_1/4<x<L_2,\\ \dfrac{L_1}{2\pi c}\ln\left[\dfrac{\tan\left(\frac{\pi}{4}+\frac{\pi(x-L_2)}{L_1}\right)}{\tan\left(\frac{\pi}{4}+\frac{\pi(x_0-L_2)}{L_1}\right)}\right], & L_2\leqslant x\leqslant L.\end{cases} \tag{9}$$

The characteristic curves are shown in Fig. 2 where c has been assumed equal to 1.

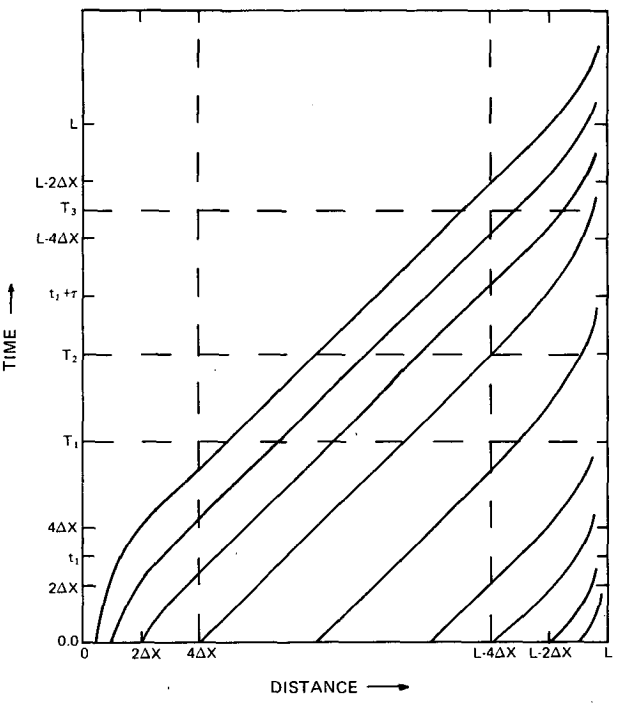

FIG. 2. Characteristic curves for the modified linear advection equation (9). Note times T_1 and T_2 are times referred to in Fig. 3; times T_1, T_2, and T_3 are times used in Fig. 7; times t_1 and $t_1+\tau$ are used in the boundary forcing of Eqs. (11) and (12).

These curves can be used to predict the future x-distribution of an initial h field by simply mapping h points at $t=0$ onto h points at some future time, $t=T$. If the initial state is a simple sinusoidal wave as shown in Fig. 3, h at time T is shortened in length, while the amplitude is preserved. Fig. 3 shows a wave at times T_0, T_1, and T_2 which are noted on Fig. 2. Thus, as can be seen from this linear analytic example, the sponge boundary condition has the property of transforming long- and medium-length waves into short waves.

2) Linear finite-difference solution

To illustrate this process in finite-difference space, Eq. (3) is transformed by using fourth-order-in-space, leapfrog-in-time difference approximations. This scheme is linearly stable if $c\Delta t/\Delta x \leqslant 1$. All cases were run on a $64\Delta x$ grid with $c\Delta t/\Delta x=0.472$, $c=300$ m s^{-1}. A useful tool for closer inspection of the effect of the boundaries is the "energy amplification," which is defined as

$$\text{Energy amplification } (\lambda^{\#})=\frac{\text{Present energy } (\lambda^{\#})}{\text{Initial energy } (\lambda^{\#})},$$

where the energy is defined as $h^2(\lambda^{\#})/2.0$. This quantity is calculated for each wavenumber $\lambda^{\#}$.

The first experiment illustrates the effect of the finite-difference approximations using cyclic boundary conditions. The initial and subsequent wave forms, and energy amplification vs wavenumbers, are shown in Fig. 4. Note that in general the energy in each wavenumber is approximately preserved with the largest error in the high wavenumbers (short wavelength). In this case, wavenumber 16 corresponds to a $4\Delta x$ wave, while wavenumber 32 corresponds to a $2\Delta x$ wave. This figure shows the changes and energy shifts that can be expected from the finite-difference scheme without boundary effects.

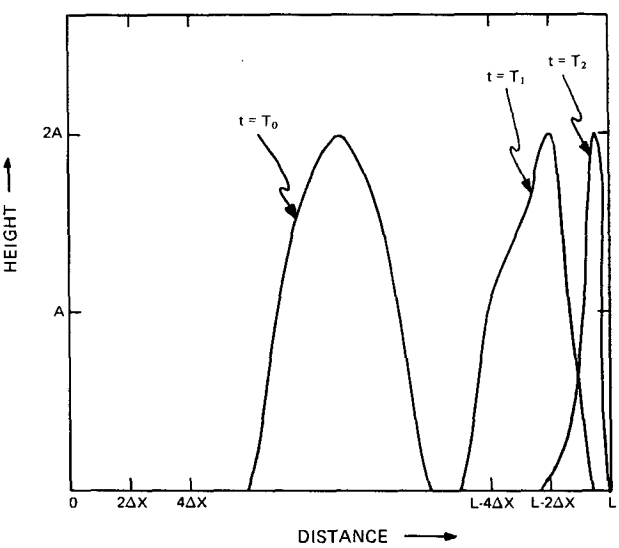

FIG. 3. Initial height field at T_0 and the height field at T_1 and T_2 as predicted from the characteristic curves in Fig. 2.

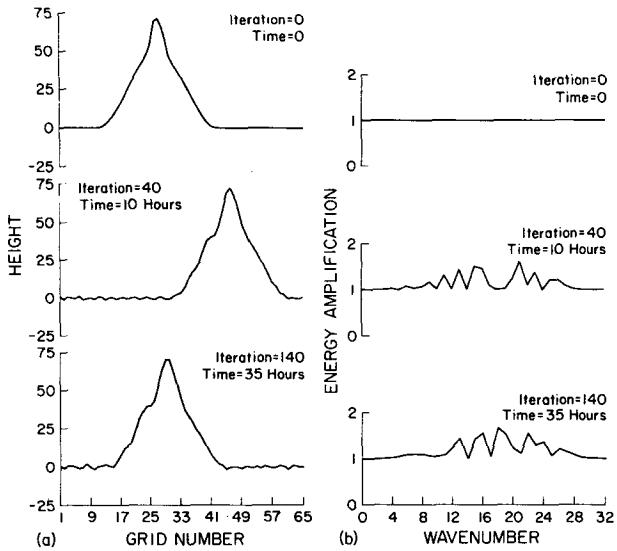

FIG. 4. (a) Height (m), and (b) energy amplification fields for the linear advection test with periodic boundaries: initial state, after 40 iterations, and after 140 iterations.

Next, the cyclic boundary is replaced with the time-dependent boundary condition with the large-scale tendency set to zero. Using the same initial wave as in the previous case (Fig. 4), the calculations shown in Fig. 5 result. During the first 40 iterations, the long waves are treated very much like they were by the cyclic boundary case; however, the short wave does show some insignificant differences. This could be because the Fourier transform routine used in the wavenumber diagnostic analysis assumes periodicity, while the data are not periodic with the sponge boundary condition.

As the wave hits the boundary (80 iterations), the energy in the long wavelengths decreases while that in the short wavelength increases. By 140 iterations very little energy remains in wavenumbers below 4 ($16\Delta x$) and a major portion of the energy is in wavenumbers above 16 ($4x\Delta$). Thus, the conclusions of the analytic solution are repeated for the linear finite-difference (advection) solution: i.e., the lateral boundary condition transforms long waves into short waves.

To complete the boundary condition, a filter is needed which removes short wave energy near the boundary. One example of such a filter is the smoother-desmoother discussed by Shuman (1957) and Shapiro (1970). This filter is used in this section, while a fourth-derivative filter is demonstrated in the nonlinear example in Section 3b. A three-point scheme is formulated as follows:

$$h_i=h_i+k_s(h_{i+1}-2h_i+h_{i-1}),$$

where k_s equals 0.25 during the first pass (smoothing) and -0.26 during the second pass (desmoothing). The

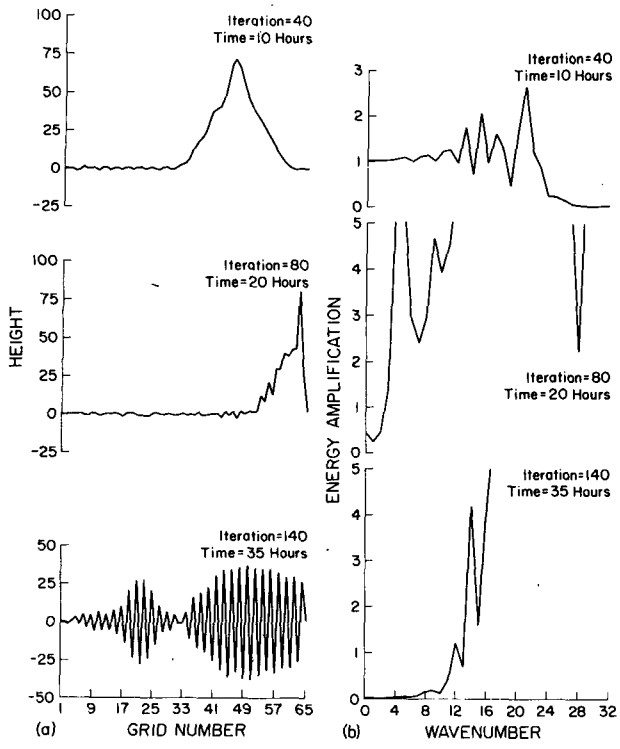

FIG. 5. (a) Height (m) and (b) energy amplification fields for the linear advection test with sponge boundaries: after 40 iterations, after 80 iterations, and after 140 iterations.

first pass of the smoother removes energy from almost all wavenumbers. For example, 11% of the energy is removed from wavenumber 4($16\Delta x$). After desmoothing, wavenumber 4 contains 99% of its original energy, i.e., the second pass restored 10% of the energy removed by smoothing. However, approximately 100% of the energy in wavenumbers 28 to 32 is removed by both passes. After 40 passes of the two-pass filter, however, wavenumber 4 has 24% of its energy removed. Thus, even with a reasonably peaked filter response, many passes remove significant energy from waves of length up to $16\Delta x$.

The next experiment combines the time-dependent boundaries as used in the previous test with the smoother-desmoother; the results are shown in Fig. 6. The smoothing routine is used on the boundary (grid points 2–7 and 58–63) every fifth and tenth time step, while it is applied to the full grid every fifteenth time step. Thus, after 20 iterations the boundaries have been smoothed-desmoothed three times and the entire grid one time. Comparison with Fig. 5 shows the same basic response of building short waves as the wave passes through the boundary; however, the energy is removed before it can reflect into the interior, as it did in the case without the filter. Therefore, after 140 iterations, very little energy remains in the grid. The combined boundary conditions and filter have acted as if the wave had passed through the boundary and out of the grid.

b. Nonzero large-scale tendencies

1) LINEAR ANALYTIC SOLUTION

For this case, the linear advective equation can be modified to yield a semi-linear equation of the following form:

$$\frac{\partial h}{\partial t}+cW(x)\frac{\partial h}{\partial x}=[W(x)-1]F(t,x). \tag{10}$$

The large-scale boundary forcing $F(t,x)$ is chosen so that a wave of the form

$$h(t,x)=\frac{A}{2}\left\{1-\cos\frac{2\pi}{L_3}[x-c(t-t_1)]\right\} \tag{11}$$

enters the grid from the left boundary, beginning at time $t=t_1$. Thus, $F(t,x)$ is

$$F(t,x)=-\frac{A\pi}{\tau}\sin\frac{2\pi}{L_3}[x-c(t-t_1)] \tag{12}$$

for $t_1\leqslant t\leqslant t_1+\tau$ and $0\leqslant x\leqslant L_1/4$. Elsewhere $F(t,x)=0$. The period of the imposed wave is $\tau=L_3/c$.

As before, the characteristic curves are described by Eqs. (7) and (9). In this case these x-t space curves are

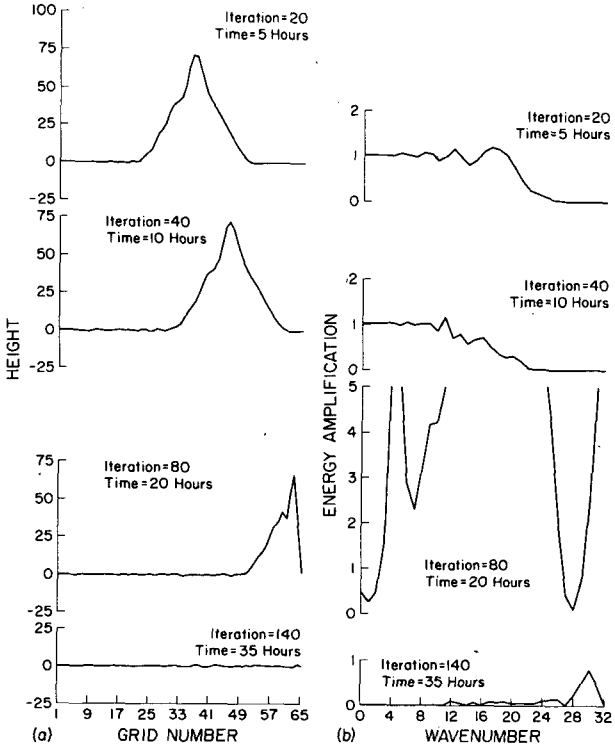

FIG. 6. (a) Height (m) and (b) energy amplification fields for the linear advection test with sponge boundaries and smoother-desmoother filtering: after 20 iterations, after 40 iterations, after 80 iterations, and after 140 iterations.

solutions along which

$$\frac{dh}{dt}=[1-W(x)]F(t,x). \tag{13}$$

Eqs. (8), (12), and (13) combine to give an ordinary differential equation for dh/dt which can be numerically integrated using Gaussian quadrature formulae. Again, as with the analytic solutions in Section 2a, the solutions shown in Fig. 7 are for times T_1, T_2, and T_3. The dashed solution curve shows the true position and form of the wave which would have resulted if the grid has extended to the left a distance L_3 and the wave had advected, without distortion, to its position at time T_3. As can be seen, the effects of the boundary condition on the phase and form are minimal. Only a slight widening of the peak has occurred, while the wavelength and phase speed have undergone almost no change.

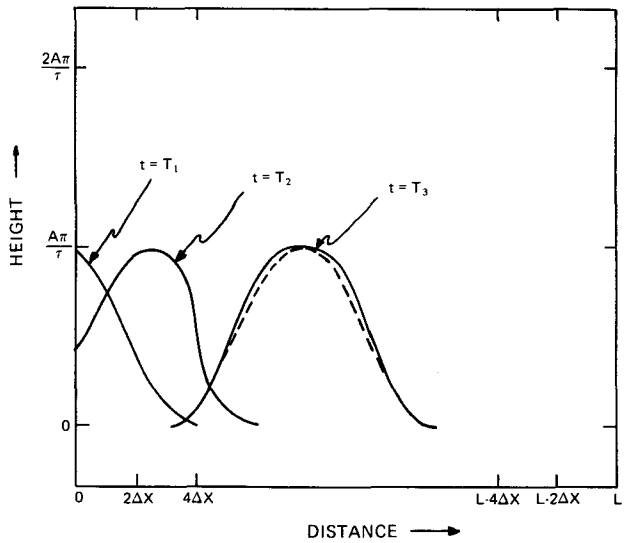

FIG. 7. Analytic solutions of the linear advection equation with time-dependent boundaries at times T_1, T_2, and T_3. Dashed curve is solution without boundaries assuming an extended grid.

2) NONLINEAR FINITE-DIFFERENCE SOLUTION

As a simple test of the time-varying boundaries, the nonlinear advective equation has been chosen:

$$\frac{\partial h}{\partial t}=-h\frac{\partial h}{\partial x}. \tag{14}$$

Eq. (14) is transformed into finite-difference space by fourth-order centered-in-space and leapfrog differencing. As before, a wavelength-dependent filter is necessary; in this case, $-k_4\partial^4 h/\partial x^4$ is added to the right-hand side of Eq. (14) .The linear stability analysis for the fourth-derivative filter dictates that

$$\beta_4=\frac{2k_4\Delta t}{\Delta x^4}\leqslant\frac{1}{16}$$

when the filter term is lagged in time; i.e., when it is evaluated at the $\tau-1$ time level while the advective term is evaluated at the τ time level. The values of k_4 have been chosen so as to have increased filtering on the edges (grid points B_l+2 through B_l+5 and B_r-5 through B_r-2), i.e., $\beta_4=0.005$ for grid points B_l+7 through B_r-7 and $\beta_4=0.060$ for grid points B_l+2 through B_l+5 and B_r-5 through B_r-2. At grid points B_l+6 and B_r-6, the average of the above β_4's is used, i.e., $\beta_4=0.0325$.

In this discussion, B_r refers to the right boundary, while B_l refers to the left. At grid points B_l+1 and B_r-1, a second-derivative diffusive filter ($k_2\partial^2 h/\partial x^2$) is employed which is also lagged in time. Stability analysis for this filter dictates that

$$\beta_2=\frac{2k_2\Delta t}{\Delta x^2}<\frac{1}{4}.$$

The damping coefficient for the second-derivative filter has been matched in such a way that the $2\Delta x$ damping is the same for both filters; thus $\beta_2=0.24$. The results of these damping terms are similar to those using the smoother-desmoother as used in the previous section.

The results of this case are shown in Fig. 8. The initial state is the same as for the linear advective case except that the amplitude has been reduced in half. By 30 h, a wave with an amplitude of 25 m has entered the grid from the left, while the initial interior wave has nearly exited on the right boundary. The right boundary does not change during this time; i.e., the interior wave can be thought of as a small-scale wave generated by a fine-mesh model, while the entering wave is a large-scale wave generated by a large-scale synoptic model. As the imposed wave reaches the right-hand boundary, this boundary begins to change as imposed by the large-scale model. Note that the boundary response is not exactly in phase with the approaching wave. This is due to modification of the wave velocity by the smaller-scale resolution of the fine-mesh model. Exact agreement is not necessary; in fact, results would not appear very different if the right boundary remained constant during the approach of this wave, just as it did as the interior wave approached. However, there is less reflection of short-wave noise when the difference between the model-calculated values and the imposed values are small; so it is advantageous to try to minimize this difference. From the state at 60 h, it is apparent that the boundary has allowed both the interior-generated wave and the exterior-imposed wave to exit with very little reflection into the grid domain.

4. Gravity wave tests

The shallow-water equations are used to examine the effect of the boundary conditions on gravity waves. We

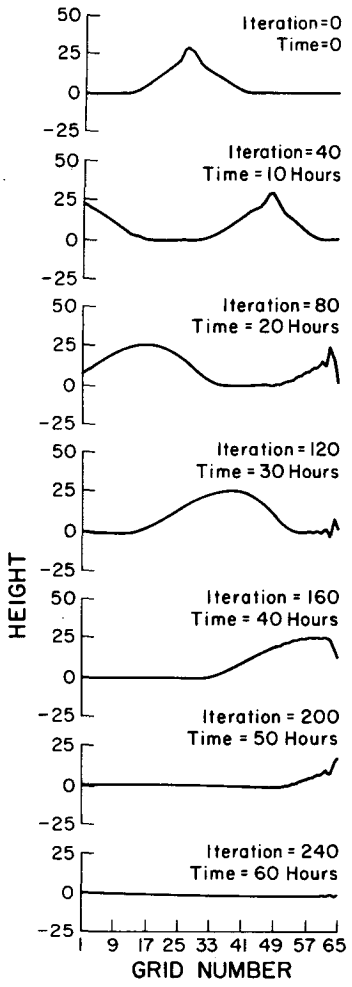

FIG. 8. Height (m) fields for the nonlinear advection equation with time-dependent boundaries and fourth-derivative filtering.

have

$$\frac{\partial u}{\partial t}+u\frac{\partial u}{\partial x}+g\frac{\partial h}{\partial x}=0$$

and (15)

$$\frac{\partial h}{\partial t}+u\frac{\partial h}{\partial x}+h\frac{\partial u}{\partial x}=0.$$

A linear perturbation analysis indicates that the propagation phase speed for the gravity wave is

$$c_g=U\pm\sqrt{gH},$$

where U is the mean velocity and H is the mean height. Application of the boundary condition to both the u and h fields yields

$$c_g=W(x)[U\pm\sqrt{gH}],$$

where $W(x)$ is the analytic boundary weighting function as used in Sections 2 and 3. Thus the wave phase speeds are slowed down as the wave enters the boundary region and become identically zero at the boundary. This is similar to the effect of the boundary condition on the advective wave speed.

To test the finite-difference analog, Eqs. (15) are transformed into finite-difference space using second-order-in-space, leapfrog-in-time difference approximations. An initial height and velocity wave is present in the domain interior (see Fig. 9). The wave is assumed to be generated interior to the small-scale grid domain and therefore was not present in the large-scale calculations. Upon starting the integration, a large-scale wave with an amplitude of 250 m is forced to enter through the left-hand boundary. The filtering is accomplished by employing the smoother-desmoother every fifth time step on the boundaries (B_l to B_l+7 and B_r-7 to B_r) and every fifteenth time step in the interior.

As the initial interior wave arrives at the right-hand side, the imposed large-scale boundary condition does not react; it does not expect the arrival of the wave since it was assumed to be generated on the small-scale grid only. However, this does not cause any noticeable reflection problem.

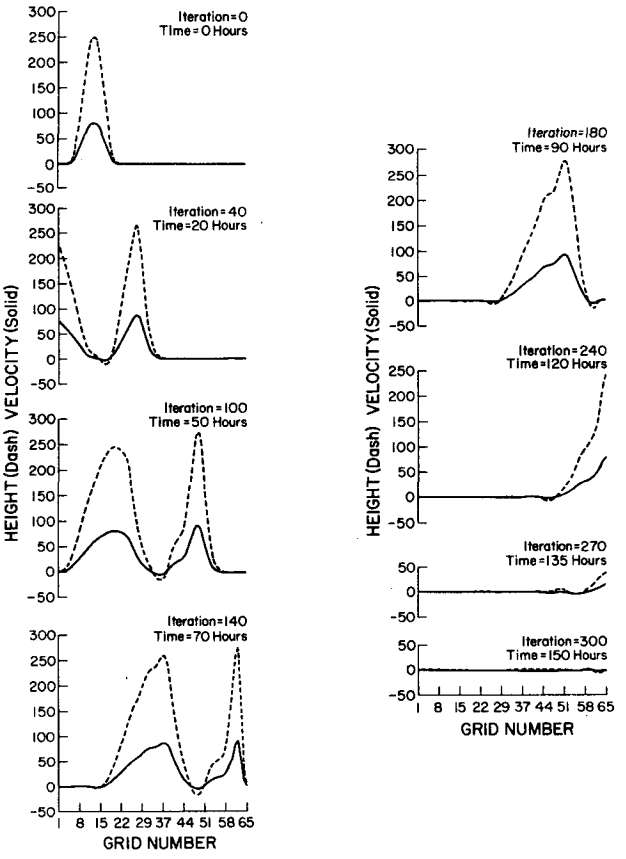

FIG. 9. Height (m) (dashed) and velocity (0.1 m s^{-1}) (solid) fields for the nonlinear shallow-water equations with time-dependent boundaries and smoother-desmoother filtering.

The large-scale wave has almost cleared the boundary region by iteration 100; its amplitude is 249 m. Thus, the boundary has caused only slight degradation of the incoming wave. As the waves move across the grid, the height and velocity gradients steepen on the front edge due to the nonlinearity in the system.

In contrast to the interior-wave boundary condition, the large-scale forced boundary condition does expect the large-scale wave, but it expects the wave at the wrong time due to the difference in propagation speed between the large-scale and small-scale grids. The wave arrives before it is expected by the boundary, but this causes little difficulty. By 300 time steps, both waves appear to have exited the grid domain with very little disturbance left behind.

5. Primitive equation tests

To test the applicability of the boundary system in a complex meteorological forecast model, a dry, two-dimensional, hydrostatic, primitive equation (PE) model is employed. The PE model includes the predictive equations for temperature, both horizontal wind components, and pressure at the top. Pressure at all other levels, density, and vertical velocity are diagnosed. For these tests a temperature tendency field is specified during the first 180 min of the integration in order to generate a solenoidal circulation and accompanying gravity waves.

The basic forecast equations are

$$\frac{\partial u}{\partial t}=-\mathbf{V}\cdot\nabla u-w\frac{\partial u}{\partial z}+fv-\frac{1}{\rho}\frac{\partial p}{\partial x}, \tag{16}$$

$$\frac{\partial v}{\partial t}=-\mathbf{V}\cdot\nabla v-w\frac{\partial v}{\partial z}-fu-\frac{1}{\rho}\frac{\partial p}{\partial y}, \tag{17}$$

$$\frac{\partial T}{\partial t}=-\mathbf{V}\cdot\nabla T-w\frac{\partial T}{\partial z}-\frac{1}{c_p}\left[gw-\frac{1}{\rho}\left(\frac{\partial p}{\partial t}+\mathbf{V}\cdot\nabla p\right)\right]+\left.\frac{\partial T}{\partial t}\right|_{\text{specified}}, \tag{18}$$

$$\left.\frac{\partial p}{\partial t}\right|_{z_t}=-\mathbf{V}\cdot\nabla p|_{z_t}+g\rho w|_{z_t}, \tag{19}$$

where the vector notation refers to the horizontal components only and the subscript z_t refers to the model top. The remaining notation is standard. The diagnostic equations are

$$\rho=\frac{p}{RT}, \tag{20}$$

$$\frac{\partial p}{\partial t}=g\rho w-g\int_z^{z_t}\nabla\cdot\rho\mathbf{V}dz-\mathbf{V}\cdot\nabla p|_{z_t}, \tag{21}$$

where ω_{z_t} has been assumed zero. Also

$$\frac{\partial w}{\partial z}=-\nabla\cdot\mathbf{V}-\frac{c_v}{c_p p}[\mathbf{V}\cdot\nabla p-\mathbf{V}\cdot\nabla p|_{z_t}]+\frac{c_v}{c_p p}\int_z^{z_t}\nabla\cdot\rho\mathbf{V}dz, \tag{22}$$

$$\frac{\partial \ln p}{\partial z}=-\frac{g}{R\bar{T}}, \tag{23}$$

where $\bar{T}$ is the layer-mean T. The differential equations are cast in a fourth-order centered-in-space and leap-frog-in-time finite-difference form. The horizontal grid interval is 120 km; the vertical grid is 1 km; and the time step is 240 s.

Initially, all fields are horizontally homogeneous, with the u, v, and w fields set to zero, i.e., initially there is no motion or horizontal gradients. The specified temperature tendency field as shown in Fig. 10 has a maximum of 5.556°C $(10^4\text{ s})^{-1}$ at 5 km (note: $10^4\text{ s}\approx 3$ h). In other words, during the 180 min the specified tendency is imposed, the temperature at 5 km is artificially warmed ~5.5°C.

Five forecasts were run with the PE model:

Case I	Periodic boundary conditions.
Case II	Time-dependent boundary conditions with all tendencies set to zero.
Case III	Time-dependent boundary conditions which were created in Case I every time step; that is, the boundary conditions were exact solutions.
Case IV	Same as Case III except the boundary tendencies were updated every fifth time step (20 min).
Case V	Same as Case III except the boundary tendencies were updated every 45 time steps (180 min).

The smoother-desmoother was applied as described in Section 4 (extra filtering was applied in the boundary regions) in all cases except Case I, which contained no extra boundary smoothing. The smoother-desmoother

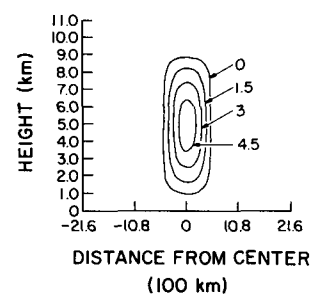

FIG. 10. Specified temperature tendency [°C $(10^4\text{ s})^{-1}$]. Maximum is 5.556.

was applied to the T, u, v, and p_{z_t} fields. The time boundary conditions as stated in Eqs. (1) and (2) were applied to these four variables in all cases except Case I.

The purpose of these tests was to 1) contrast periodic vs sponge boundary conditions (I vs II). Case II also demonstrates the stability of the boundary scheme when time varying conditions are not available; 2) show that introduction of exact boundary conditions gives exact results except for the effect of the extra boundary smoothing (I vs III); 3) examine the impact of infrequent updating of the boundary tendencies (I vs IV) and I vs V). These cases also illustrate the behavior of the boundary scheme to incorrectly specified boundary tendencies. Case IV might arise if a shorter time step were used in the interior model than in the model from which the boundary tendencies were calculated. Case V might arise if the external specified tendencies were only available every 180 min.

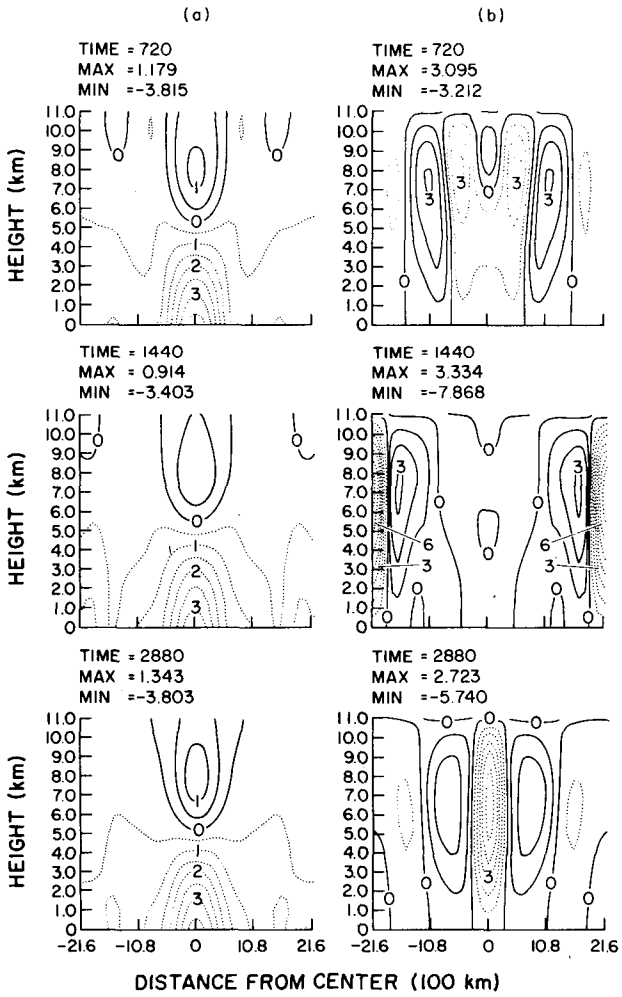

FIG. 11. (a) Pressure perturbation (mb) with contour interval equal to 0.5 and (b) vertical velocity (cm s^{-1}) with contour interval of 1.0 at 720, 1440, and 2880 min for Case I. Dotted contours denote negative values.

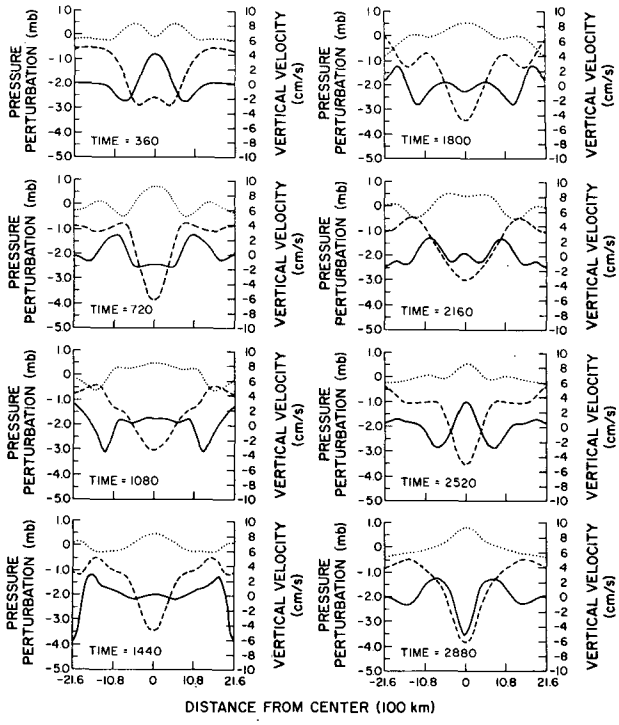

FIG. 12. The 0.1 km pressure perturbation (dashed), 11.0 km pressure perturbation (dotted), and 5.0 km vertical velocity (solid) at 360, 720, 1080, 1440, 1800, 2160, 2520, and 2880 min for Case I.

Figs. 11 and 12 depict the results of Case I. Figs. 11 shows the 720, 1440, and 2880 min pressure perturbation and vertical velocity fields. The pressure perturbation for all cases is defined as the difference between the initial pressure at a grid point and the current pressure at the same grid point. Fig. 12 shows the 0.1 km and 11.0 km pressure perturbation and the 5.0 km vertical velocity traces. As can be seen, a surface low and upper-level high dipole were created by the imposed temperature change during the first 180 min of the forecast. Two gravity waves propagate outward from the grid center when the imposed temperature change is shut off. By 1080 min the wave has hit the boundary. Due to the periodic boundaries these waves re-enter the grid and propagate back toward the grid center. At 2520 min the wave is in nearly the same position as it was at 360 min.

Case II results are shown in Figs. 13 and 14. Recall this case has zero large-scale tendencies. Note at 720 min the maximum and minimum pressure perturbation values differ by ~15% from those in Case I, while the vertical velocity values agree within 1%. This case is very similar to Case I until the gravity waves enter the boundary regions at approximately 1080 min. At this time boundary conditions begin to break down the wave and remove it via the smoother-desmoother. By

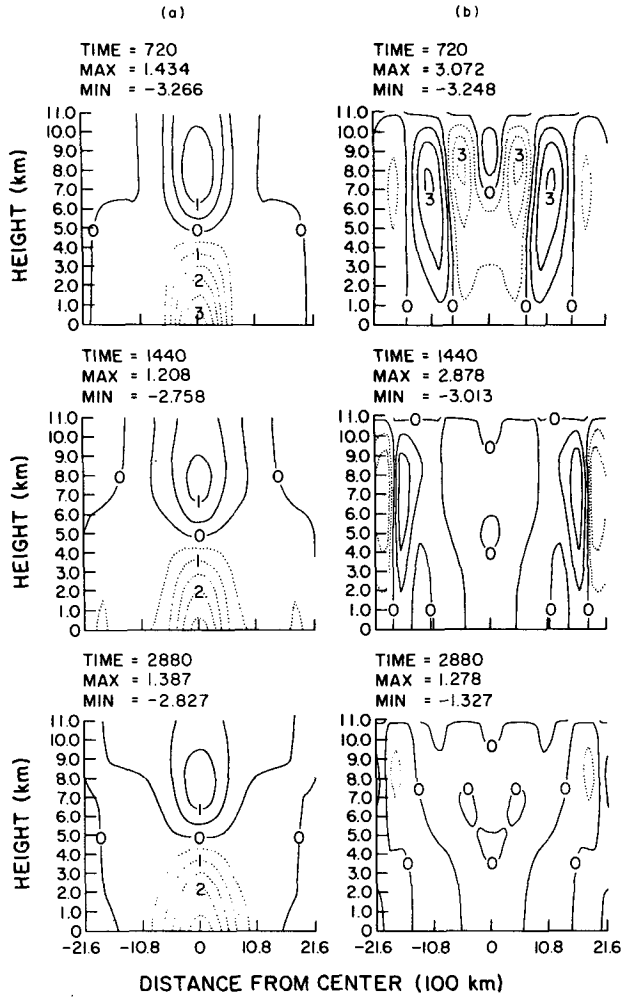

FIG. 13. (a) Pressure perturbation (mb) with contour interval equal to 0.5 and (b) vertical velocity (cm s^{-1}) with contour interval of 1.0 at 720, 1440, and 2880 min for Case II. Dotted contours denote negative values.

2160 very little of the gravity waves remains, i.e., the waves appear to have exited the domain leaving the surface low, upper-level high pressure pattern with nearly zero vertical motion. This implies that the horizontal winds are in nearly geostrophic equilibrium with the mass field. This is also suggested by the pressure tendency, which decreased from a maximum at 2160 min of $\sim$0.6 mb $(10^4 \text{ s})^{-1}$ to a 2880 min maximum of 0.2 mb $(10^4 \text{ s})^{-1}$.

Cases I and II show the response of a PE model to an impulse of diabatic heating such as might be produced by the release of potential instability (Kreitzberg and Perkey, 1976). The 5.5°C forced temperature change produces a stationary surface low of about 3 mb (Case II, Fig. 14, 2880 min) plus gravity waves with a surface pressure fluctuation $\sim$1 mb. The vertical velocity associated with the stationary low is very small (Case II, Fig. 14, 2880 min), while both gravity waves have a vertical velocity amplitude of $\sim$2 cm s^{-1}; these add to give 4 cm s^{-1} at 360 and 2520 min in Case I, Fig. 12.

Case III vs Case I illustrates the response when the boundary tendencies are specified exactly (every time step). Comparing Figs. 15 and 16 with Figs. 11 and 12, one can see that the circulations are basically identical. The 5% to 10% differences are explained by the increased boundary region smoothing through which the waves in Case III had to traverse. It is evident that the scheme allowed the exiting waves to leave the grid domain as in Case II and the entering waves to proceed into the domain with only slight degradation due to the increased viscosity in the boundary region. In general, the amount of degradation experienced by an incoming wave will be inversely proportional to its wavelength, i.e., incoming short waves will be damped more than longer waves. The damping response would be expected to behave similar to the response of the filter scheme used in the boundary region.

Case IV results (Fig. 17) again exhibit no significant changes from Case I or Case III. Therefore, if the specified tendencies are not known as frequently as is needed by the interior model, these results suggest that no serious problems will arise. As stated earlier, Case IV might arise when the boundary specified tendencies for a fine-grid, short-time-step, mesoscale model are being supplied by a coarse-grid, long-time-step, large-scale model. In the more extreme case where the tendencies are only available every 180 min from 180 min coarse-grid model histories, or from 180 min sounding analyses, Case V (not shown) pointed to an expected limitation. Again this case proved to be stable, and the results were very similar to those presented above until the waves tried to re-enter the grid; at that point they became very different from the above cases. For example, the 2880 min vertical velocity had a minimum on the order of -1.5 cm s^{-1} as opposed to the -5 cm s^{-1} in Case I. This decrease in wave amplitude resulted from the severe frequency smoothing due to the 180 min boundary updating. Note that the period of the above

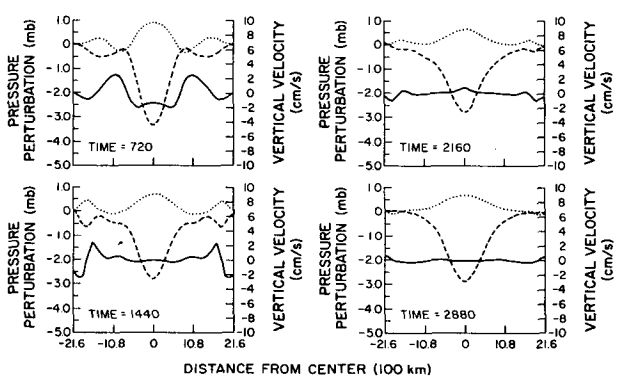

FIG. 14. The 0.1 km pressure perturbation (dashed), 11.0 km pressure perturbation (dotted), and 5.0 km vertical velocity (solid) at 720, 1440, 2160, and 2880 min for Case II.

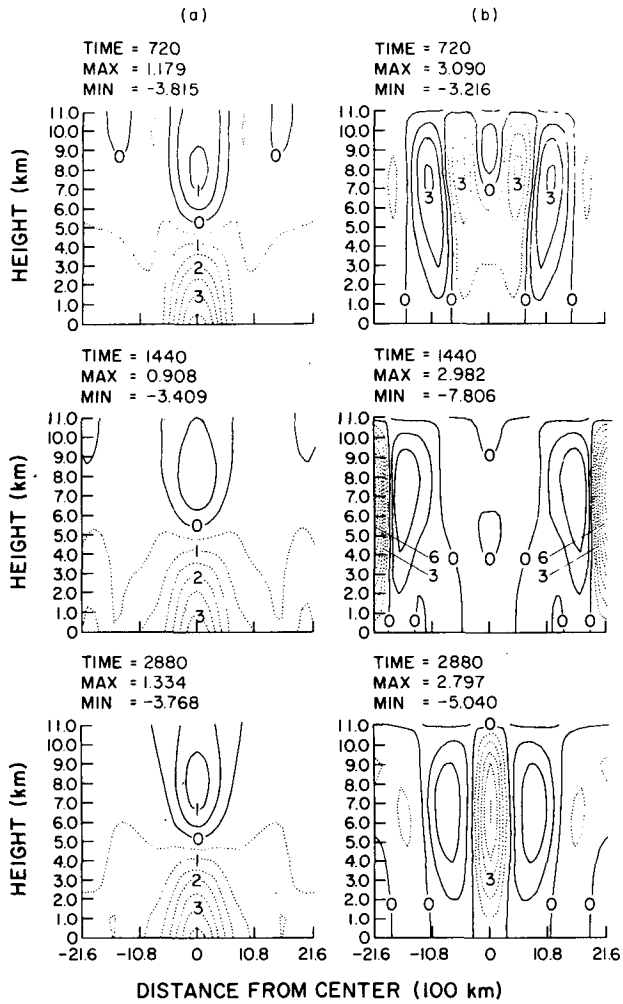

FIG. 15. (a) Pressure perturbation (mb) with contour interval equal to 0.5 and (b) vertical velocity (cm s^{-1}) with contour interval of 1.0 at 720, 1440, and 2880 min for Case III. Dotted contours denote negative values.

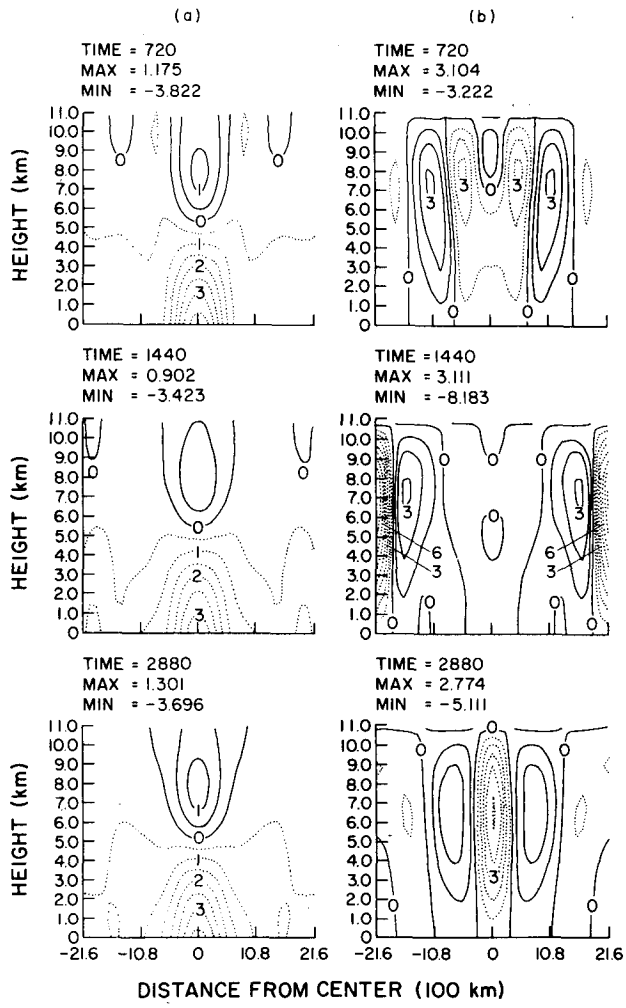

FIG. 17. (a) Pressure perturbation (mb) with contour interval equal to 0.5 and (b) vertical velocity (cm s^{-1}) with contour interval of 1.0 at 720, 1440, and 2880 min for Case IV. Dotted contours denote negative values.

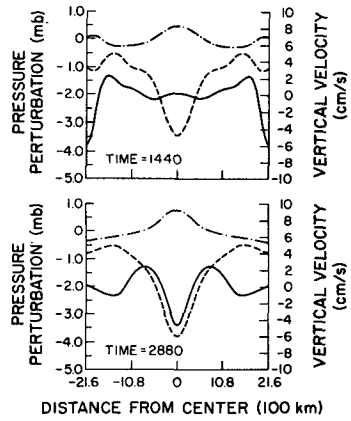

FIG. 16. The 0.1 km pressure perturbation (dashed), 11.0 km pressure perturbation (dot-dashed), and 5.0 km vertical velocity (solid) at 1440 and 2880 min for Case III.

waves is approximately 100 min; thus, a sampling rate of 180 min is not sufficient to preserve the amplitude of this wave with any degree of realism. Therefore, caution must be used when the boundary forcing update frequency is selected to assure that this frequency does not overfilter so that the desired boundary information is lost. The boundary scheme will remain stable but the results will not be reasonable. This, of course, is not a problem with just this scheme but is inherent in any boundary specification one might choose.

6. Summary and conclusions

The need exists for time-dependent lateral boundary conditions which can be used with limited-area primitive equation models; these conditions should reflect

developments on the large scale. A practical lateral boundary system has been developed which utilizes large-scale model forecasts on the boundary of the limited-area model domain, thereby permitting the limited-area forecast to incorporate changes in the large-scale conditions.

Using large-scale tendencies linearly combined with limited-area forecast tendencies, time-dependent lateral boundary conditions are introduced into the limited-area model. It has been demonstrated that the prescribed combination transforms existing long- and medium-length advective and gravity waves into short waves which can then be removed by a low-pass filter. Incoming waves are modified only slightly by the boundary system.

This paper demonstrates how these boundary conditions react to advective and gravity waves in idealized cases. It also suggests how they will work in more complex meteorological models including Rossby waves. This scheme has been used in a fully moist, three-dimensional, primitive equation model for real-data forecasts (Kreitzberg *et al.*, 1974). The use of this lateral boundary condition system yields a practical solution to the problem of specifying the boundary values of meteorological parameters in a limited-area forecast model. The system's properties make it applicable for use in regions which have significant externally-generated large-scale changes over the forecast domain and period.

Acknowledgments. This work was performed under Project THEMIS Contract AF19628-69-C-0092 and Energy Research and Development Agency Grant E(11-1)-2360. Also, computer time was made available through the National Center for Atmospheric Research (NCAR) Computing Facility.

The authors wish to thank Drs. Paul Gordon (Drexel University) and Joseph Klemp (NCAR) for their helpful and valuable suggestions. Also, Donald Perkey wishes to acknowledge the advice and criticism of Drs. A. Blackadar, R. Anthes, J. Hovermale, and H. Panofsky who, as members of his doctoral committee at The Pennsylvania State University, reviewed the research in this paper.

REFERENCES

Cooley, D. S., 1973: Fundamental changes in the grid structure and boundary conditions in the limited-area fine-mesh (LFM) model. NOAA Tech. Procedures Bulletin No. 82, NWS/Weather Analysis and Prediction Division, Silver Spring, Md.

Davies, H. C., 1972: On the lateral boundary conditions for the primitive equations. *J. Atmos. Sci.*, **30**, 147–150.

Kesel, P. G., and F. J. Winninghoff, 1972: The Fleet Numerical Weather Central operational primitive equation model. *Mon. Wea. Rev.*, **100**, 360–373.

Kreitzberg, C. W., and D. J. Perkey, 1976: Release of potential instability: Part I. A sequential plume model within a hydrostatic primitive equation model. *J. Atmos. Sci.*, **33**, 456–475.

——, —— and J. E. Pinkerton, 1974: Mesoscale modeling, forecasting and remote sensing research. Project THEMIS Final Report, AFCRL-TR-74-0253, Dept. of Physics and Atmos. Sci., Drexel University, 318 pp. [Available from NTIS, ref: AD-784-875].

Oliger, J., and A. Sundström, 1976: Theoretical and practical problems in formulating boundary conditions for a limited-area model. Dept. Computer Sci., Stanford Univ., Stanford, Calif. (manuscript in preparation).

Shapiro, M. A., and J. J. O'Brien, 1970: Boundary conditions for fine-mesh limited-area forecasts. *J. Appl. Meteor.*, **9**, 345–349.

Shapiro, R., 1970: Smoothing, filtering and boundary effects. *Rev. Geophys. Space Phys.*, **8**, 359–387.

Shuman, F. G., 1957: Numerical methods in weather prediction: II. Smoothing and filtering. *Mon. Wea. Rev.*, **85**, 357–371.

Sundström, A., 1973: Theoretical and practical problems in formulating boundary conditions for a limited-area model. Institute of Meteorology, University of Stockholm, Report DM-9, May 1973.

Williamson, D. L., and G. L. Browning, 1974: Formulation of the lateral boundary conditions for the NCAR limited area model. *J. Appl. Meteor.*, **13**, 8–16.